

REPORT DOCUMENTATION PAGE				Form Approved OMB No. 0704-0188	
Public reporting burden for this collection of information is estimated to average 1 hour per response, including the time for reviewing instructions, searching existing data sources, gathering and maintaining the data needed, and completing and reviewing this collection of information. Send comments regarding this burden estimate or any other aspect of this collection of information, including suggestions for reducing this burden to Department of Defense, Washington Headquarters Services, Directorate for Information Operations and Reports (0704-0188), 1215 Jefferson Davis Highway, Suite 1204, Arlington, VA 22202-4302. Respondents should be aware that notwithstanding any other provision of law, no person shall be subject to any penalty for failing to comply with a collection of information if it does not display a currently valid OMB control number. PLEASE DO NOT RETURN YOUR FORM TO THE ABOVE ADDRESS.					
1. REPORT DATE (DD-MM-YYYY) 28-08-2009		2. REPORT TYPE Technical Paper		3. DATES COVERED (From - To)	
4. TITLE AND SUBTITLE A Plume Comparison of Xenon and Krypton Propellant on a 600 W Hall Thruster				5a. CONTRACT NUMBER	
				5b. GRANT NUMBER	
				5c. PROGRAM ELEMENT NUMBER	
6. AUTHOR(S) Michael R. Nakles & Ryne R. Barry (ERC); C. William Larson & William A. Hargus (AFRL/RZSS)				5d. PROJECT NUMBER	
				5e. TASK NUMBER	
				5f. WORK UNIT NUMBER 33SP0706	
7. PERFORMING ORGANIZATION NAME(S) AND ADDRESS(ES) Air Force Research Laboratory (AFMC) AFRL/RZST 4 Draco Drive Edwards AFB CA 93524-7160				8. PERFORMING ORGANIZATION REPORT NUMBER AFRL-RZ-ED-TP-2009-326	
9. SPONSORING / MONITORING AGENCY NAME(S) AND ADDRESS(ES) Air Force Research Laboratory (AFMC) AFRL/RZS 5 Pollux Drive Edwards AFB CA 93524-7048				10. SPONSOR/MONITOR'S ACRONYM(S)	
				11. SPONSOR/MONITOR'S NUMBER(S) AFRL-RZ-ED-TP-2009-326	
12. DISTRIBUTION / AVAILABILITY STATEMENT Approved for public release; distribution unlimited (PA #09405).					
13. SUPPLEMENTARY NOTES For 31 st International Electric Propulsion Conference (IEPC 09) to be held in Ann Arbor, MI from 20-24 September 2009.					
14. ABSTRACT An experimental study was conducted to compare variations in the plume of a 600 W Hall effect thruster operating on xenon and krypton propellants. Both a guarded Faraday probe and a retarding potential analyzer were used to measure plume properties for various thruster operating conditions. Discharge current data was also measured in the time domain using an oscilloscope and in the frequency domain using a signal analyzer for all tested operating conditions. Operating conditions were chosen to provide a comparison of the effects of radial magnetic field strength for both propellants. For each xenon propellant operating condition, two krypton propellant operating conditions were tested. One condition matched volumetric flow rate and the other condition matched anode power by increasing the anode flow rate. The plume data were analyzed to calculate various components of the energy and propellant utilization efficiencies as defined in Ref. 1. Faraday probe data were used to calculate the divergence and beam current utilization efficiencies. Voltage utilization efficiency was calculated using data from the retarding potential analyzer. Compared with xenon, krypton divergence efficiency is approximately 15-20% lower and its current utilization efficiency is 5-10% lower. Differences between voltage utilization efficiency for xenon and krypton were small. Anode current oscillation magnitude was lower for krypton propellant.					
15. SUBJECT TERMS					
16. SECURITY CLASSIFICATION OF:			17. LIMITATION OF ABSTRACT SAR	18. NUMBER OF PAGES 22	19a. NAME OF RESPONSIBLE PERSON Dr. William A. Hargus Jr
a. REPORT Unclassified	b. ABSTRACT Unclassified	c. THIS PAGE Unclassified			19b. TELEPHONE NUMBER (include area code) N/A

A Plume Comparison of Xenon and Krypton Propellant on a 600 W Hall Thruster

Michael R. Nakles*, Ryne R. Barry†

ERC, Inc., Edwards Air Force Base, CA 93524

C. William Larson*, and William A. Hargus, Jr.*

Air Force Research Laboratory, Edwards Air Force Base, CA 93524

An experimental study was conducted to compare variations in the plume of a 600 W Hall effect thruster operating on xenon and krypton propellants. Both a guarded Faraday probe and a retarding potential analyzer were used to measure plume properties for various thruster operating conditions. Discharge current data was also measured in the time domain using an oscilloscope and in the frequency domain using a signal analyzer for all tested operating conditions. Operating conditions were chosen to provide a comparison of the effects of radial magnetic field strength for both propellants. For each xenon propellant operating condition, two krypton propellant operating conditions were tested. One condition matched volumetric flow rate and the other condition matched anode power by increasing the anode flow rate. The plume data were analyzed to calculate various components of the energy and propellant utilization efficiencies as defined in Ref. 1. Faraday probe data were used to calculate the divergence and beam current utilization efficiencies. Voltage utilization efficiency was calculated using data from the retarding potential analyzer. Compared with xenon, krypton divergence efficiency is approximately 15-20% lower and its current utilization efficiency is 5-10% lower. Differences between voltage utilization efficiency for xenon and krypton were small. Anode current oscillation magnitude was lower for krypton propellant.

Nomenclature

e	elementary charge
I_a	anode discharge current
I_b	integrated thruster beam current
I_{m1}	magnet current to the four series outer magnetic cores
I_{m2}	magnet current to the central magnetic core
j	plume charge flux
m	atomic mass
\dot{m}_a	anode mass flow rate
P	anode power
q	multiple for units of elementary charge
r	radial distance in thruster coordinate system
V	ion acceleration voltage
\bar{V}	mean ion acceleration voltage from a distribution function
V_a	anode potential measured with respect to cathode common potential
\dot{V}_a	anode volumetric flow rate
V_0	ion retarding grid potential for retarding potential analyzer

*Research Engineer, AFRL/RZSS, 1 Ara Rd. Edwards AFB, CA 93524

†Undergraduate Student, Dept. of Aeronautics and Astronautics, MIT, Cambridge, MA 02139

Γ	current collected by retarding potential analyzer
ΔV	average ion acceleration voltage
η_a	anode efficiency
θ	angular position in thruster coordinate system
$\langle \theta \rangle_j$	charge flux weighted plume divergence angle
ϕ_{DIV}	divergence loss component of propellant utilization
ϕ_{VDF}	velocity distribution loss component of propellant utilization
$\langle \rangle_j$	charge flux weighted average quantity in the plume
$\langle \rangle_m$	mass weighted average quantity in the plume
$\langle \rangle_{mv}$	momentum weighted average quantity in the plume

Introduction

Due to a number of engineering reasons, xenon (Xe) is the propellant of choice for Hall effect thrusters. These include its high mass (131 amu) and its relatively low ionization potential (12.1 eV). Furthermore, the inert nature of xenon eliminates much of the controversy that plagued early electrostatic propulsion efforts when mercury (Hg) and cesium (Cs) were the propellants of choice. Although xenon is a noble gas, it is the most massive, and due to its non-ideal gas behavior, it is possible to pressurize and store at specific densities that exceeded unity. As such, it can be stored at higher densities than the common liquid monopropellant hydrazine.²

While xenon will likely remain the ideal propellant for electrostatic electric propulsion thrusters. There are several concerns that have driven the Hall effect thruster community to explore alternative propellants. As orbit raising missions of longer duration and larger payloads are proposed for Hall effect thrusters, the mass of required propellant increases. Xenon production is a byproduct of the fractional distillation of atmospheric gases for use primarily by the steel industry. Due to the low concentration of xenon in the atmosphere (~ 90 ppb), worldwide production appears to be limited to approximately 6,000 m³ per year. Increasing industrial demand for items such as high efficiency lighting and windows has produced wide price swings in the past decade. Xenon prices have varied by as much as a factor of ten.

For high thrust to power missions, bismuth (Bi) has been demonstrated as a viable alternative Hall effect thruster propellant. Bismuth, with its high atomic mass (209 amu) and low ionization potential (7.3 eV) appears to have advantages for missions where high thrust at reduced specific impulse is advantageous, primarily orbit raising missions. Bismuth's main drawback is that the metal must be vaporized to be ionized and accelerated within a Hall effect thruster. The requirement for high temperatures (boiling point of 1,837 K) require special engineering considerations compared to the relatively simple gas distribution systems used for xenon. In addition, the use of vapor as a propellant has tended to cause concern for spacecraft operators despite the assurances of thruster developers.

For missions that can benefit from higher specific impulse, krypton (Kr) may have some benefits. Krypton has a lower atomic mass (83.8 amu), but a higher ionization potential (14.0 eV) than xenon. However like xenon, krypton is a noble gas and could be easily integrated into existing xenon propellant management systems without much modification. The similar ionization potential would likely not dramatically affect the efficiency of a Hall effect thruster, and the lower mass would produce a 25% increase in specific impulse assuming there were no offsetting losses. The increase in specific impulse would be useful for missions such as station-keeping. For missions such as orbit raising, increasing the specific impulse will increase trip time due to power limitations. However as solar electric power system specific power decreases, increasing the specific impulse of the propulsion system is advantageous. Krypton is approximately 10 times more common in the atmosphere (and hence in production) than xenon, and when accounting for mass is approximately 6 times less expensive. One disadvantage for krypton is that its tankage fraction appears to be substantially higher than that of xenon due to reduced van der Waals interactions. As such, compressed gas tankage fractions could be as high as 37%. At least one study has examined this issue and has identified space rated cryo-coolers that could liquefy krypton (120 K boiling point), or for that matter xenon (165 K boiling point), and reduce tankage fractions to less than 2%.²

The goal of this study is to understand the differences between xenon and krypton plumes in a medium power Hall effect thruster in a design optimized for xenon. Several plume properties are measured and some generalizations of various performance parameters are inferred. However, this study is primarily an

exploratory investigation into the possibilities of using krypton as a propellant in Hall effect thrusters, primarily due to its low cost and possible application as a low-development overhead replacement for existing xenon Hall effect thruster systems.

Experimental Apparatus and Techniques

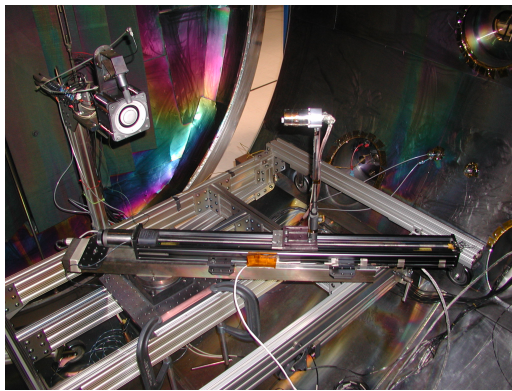
Test Facility

The tests performed in this study utilized Chamber 1 at the Air Force Research Laboratory at Edwards AFB. Chamber 1 is a cylindrical non-magnetic stainless steel vacuum chamber with a 2.4 m diameter and a 4.1 m length. Pumping is provided by two liquid nitrogen baffled (70 K), 1.2 m flanged gaseous helium two stage cryogenic (15 K) vacuum pumps with a measured pumping speed on both xenon and krypton of 48,500 L/s. Chamber pressure is monitored with a cold cathode gauge. Background pressure for thruster operation was measured to be 9×10^{-6} Torr for xenon and 7×10^{-6} Torr for krypton with gas correction factors applied.

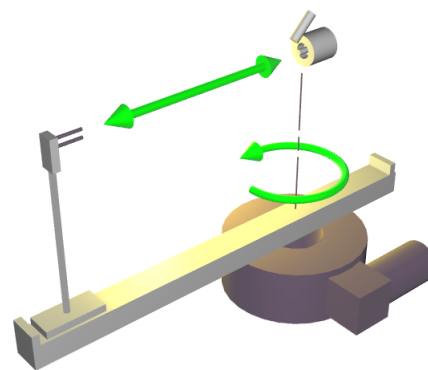
The interior of the chamber is covered with nuclear grade, low sulfur, flexible graphite 4.7 mm thick. Both chamber ends contain louvered beam dumps manufactured in-house using 13 mm thick, 15 cm wide graphite panels to reduce redeposition of sputtered materials on the thruster during extended firings. The chamber floor is protected using a carbon-carbon woven blanket that allows for ease of placement and removal.

The thruster is mounted on a 1.2 m long by 1.8 m wide test cart that is capable of traversing on internal chamber rails or being removed from the chamber using a roller system. For these tests, the thruster is mounted atop a column and cantilevered 30 cm along the chamber central axis. A stepper motor driven rotary stage is placed with its center of rotation directly below the thruster exit plane directly on the working surface of the test cart. Due to the column and cantilever placement of the thruster, the arm mounted on the rotary stage is capable of rotating between $\pm 150^\circ$ from the plume axis.

The arm mounted on the rotary stage is a stepper motor driven linear translational stage capable of traversing up to 80 cm from the center of rotation of the rotary stage. This combination of rotary and linear motion allows for the continuous sweeping of various plasma interrogation probes in the $r - \theta$ plane.



(a) Photograph of the testing environment inside of Chamber 1.



(b) The probe translation system is composed of a rotary stage for angular motion and a linear stage for radial movement.

Figure 1. Probe measurements were conducted in Chamber 1 using a stepper motor-driven translation stage system for movement.

A computer data acquisition system monitors voltages and currents of the power supplies used in Hall thruster operation. Data was sampled at a rate of 2 Hz for this study.

Hall Effect Thruster

The Hall thruster used in this study was the rectangular 600 W Busek Company BHT-HD-600 Hall thruster with a 3.2 mm hollow cathode. Photographs of the thruster are shown in Fig. 2. This thruster has a conventional five magnetic core (one inner, four outer) magnetic circuit. The acceleration channel of the thruster has a 32 mm outer radius and a 24 mm inner radius and a depth of approximately 10 mm between the

geometrical exit plane and the furthest forward extent of the anode. The thruster has been extensively characterized to have a thrust of 39 mN with a specific impulse of 1,530 s, yielding an efficiency of approximately 50% at the nominal conditions specified in Table 1.

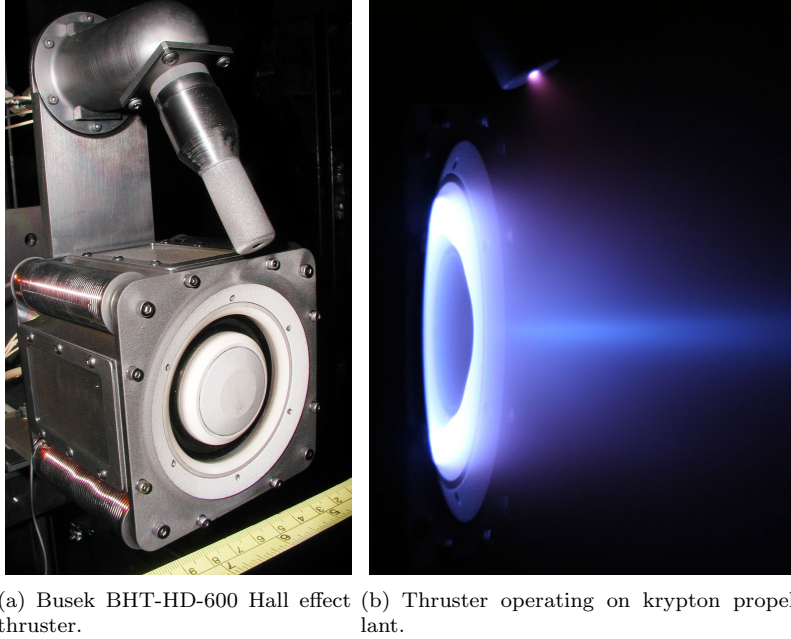


Figure 2. Photographs of the Busek BHT-HD-600 Hall effect thruster used in this study.

Guarded Faraday Probe

Ion current flux was measured using a guarded Faraday probe pictured in Fig. 3. The electrodes were constructed from molybdenum. Ion current was collected with a disk measuring 8.3 mm in diameter. A concentric guard piece, measuring 22.5 mm in outer diameter, was used to minimize the effects of the plasma sheath on the ion current collector's effective collecting area. A 0.56 mm wide gap existed between the outer wall of the collector and the inner wall of the guard ring. The effective current collector area of the probe was calculated by adding a portion of the gap surface area to the collector surface area. The amount of gap area that contributed to the effective current collector area was proportional to the ratio of lateral wall surface area of the collector to the total lateral wall surface area on both sides of the gap as suggested in Ref. 3. Ion charge flux was measured by dividing the current to the collector by its effective surface area. The disk and guard ring were biased to -30 V with respect to chamber ground during the measurements so that ion saturation was achieved. The effects of secondary electron emission were assumed to be less than a few percent⁴ and were neglected in the analysis of the measurements.

Table 1. Nominal BHT-HD-600 Hall thruster operating conditions for xenon propellant.

Parameter	Value
Anode Flow	2.45 mg/s Xe
Cathode Flow	197 μ g/s Xe
Anode Potential	300 V
Anode Current	2.16 A
Keeper Current	0.5 A
Heater Current	3.0 A

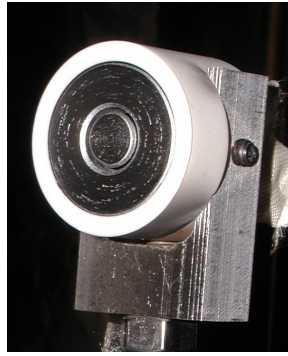


Figure 3. The guarded Faraday probe used in charge flux measurements.

Retarding Potential Analyzer

The retarding potential analyzer (RPA) used in this experimental investigation was a four grid design described in detail in Ref. 3. The RPA operates as an energy filtered Faraday probe. The energy filtering is accomplished using a series of biased grids in front of the current collector.

The first grid acts as an aperture to reduce plasma flow into probe and is allowed to float at the local plasma floating potential. The second grid (electron repulsion), biased negatively with respect to chamber ground, repels incoming electrons within the plasma while allowing ions to pass through. The potential of the ion retarding grid (third grid) is swept positively relative to chamber ground to allow selective passage of ions based on their kinetic energy. The fourth grid (electron suppression) is placed in front of the collector to suppress ion impact induced secondary electron emission.

Current to the collector is measured as a function of ion retarding grid potential. The probe current is differentiated with respect to ion retarding potential to calculate energy-per-charge distribution function. Analytically, for a single species, the derivative of the current per unit area is⁵

$$\frac{d\Gamma}{dV_0} = \frac{qe}{m} f(V) \quad (1)$$

which is proportional to the ion energy-per-charge distribution of the plasma.

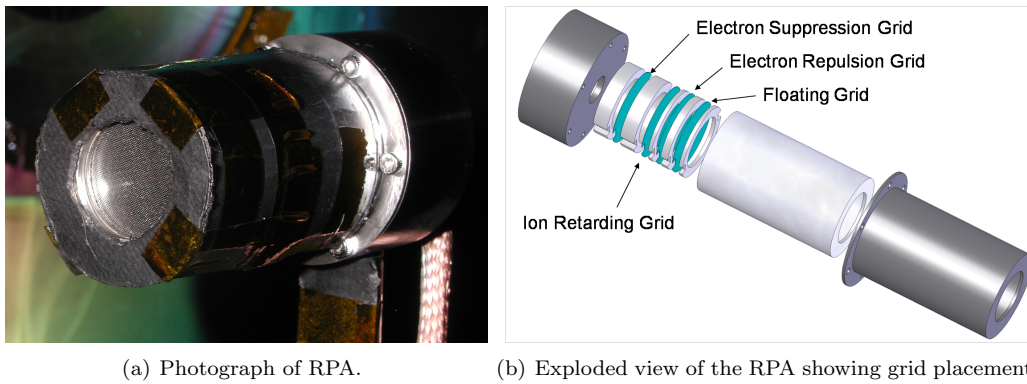


Figure 4. Retarding potential analyzer (RPA) used to measure energy distribution functions (EDF).

Performance Evaluation Techniques

Reference 1 outlines a standard methodology for Hall thruster anode efficiency analysis. This method separates anode efficiency into the product of energy efficiency and propellant utilization efficiency. The anode efficiency can be expressed as

$$\eta_a = \left(\frac{\Delta V}{V_a} \right) \left(\frac{I_b}{I_a} \right) \phi_{\text{VDF}} \phi_{\text{DIV}} \quad (2)$$

where the first two terms comprise the energy efficiency and the last two terms produce the propellant utilization efficiency. Energy efficiency accounts for losses due to Joule heating, radiation, and ionization processes. It is completely separated from jet vector properties. Propellant utilization efficiency accounts for losses due to geometric plume divergence and ion species composition.

Faraday probe measurements can be used to approximate both the charge utilization efficiency and the plume divergence efficiency. The beam current can be calculated as

$$I_b \approx \pi r^2 \int_{-\frac{\pi}{2}}^{\frac{\pi}{2}} j(\theta) |\sin \theta| d\theta \quad (3)$$

The ratio of beam current to the anode current (recorded by the data acquisition system) is the charge utilization efficiency.

Plume divergence efficiency is a measure of jet momentum loss due to beam divergence. It is defined as the ratio of axial momentum that produces thrust to the total momentum exhausted in the plume. It can be approximated using charge flux-weighted average divergence

$$\phi_{\text{DIV}} = \langle \cos \theta \rangle_{mv}^2 \approx \left(\frac{\pi r^2 \int_{-\frac{\pi}{2}}^{\frac{\pi}{2}} j(\theta) \cos \theta |\sin \theta| d\theta}{\pi r^2 \int_{-\frac{\pi}{2}}^{\frac{\pi}{2}} j(\theta) |\sin \theta| d\theta} \right)^2 = \left(\frac{I_{\text{axial}}}{I_b} \right)^2 \quad (4)$$

Voltage utilization efficiency is the ratio of average ion acceleration voltage to anode voltage. Being a part of the energy efficiency, it contains no information about the vector properties of the jet. Voltage utilization can be calculated as

$$\left(\frac{\Delta V}{V_a} \right) = \left(\frac{\langle \bar{V}(\theta) \rangle_m}{V_a} \right) \approx \frac{1}{V_a} \left(\frac{\pi r^2 \int_{-\frac{\pi}{2}}^{\frac{\pi}{2}} j(\theta) \bar{V}(\theta) |\sin \theta| d\theta}{\pi r^2 \int_{-\frac{\pi}{2}}^{\frac{\pi}{2}} j(\theta) |\sin \theta| d\theta} \right) \quad (5)$$

where a charge flux-weighted approximation enables calculation through a combination of RPA and Faraday probe data.

Results and Discussion

Magnetic Field Effects

Probe measurements were taken for four different magnetic field strength configurations for each propellant. Varying the magnetic field by changing the applied current to the four series connected outer magnetic cores (m1) and the central core (m2) changed both the plume focusing and anode current oscillatory conditions. Three of these conditions have been tested in the past with xenon.⁶⁻⁸ The $I_{m1} = 4.00$ A, $I_{m2} = 4.00$ A case has the strongest radial magnetic field strength. The $I_{m1} = 4.00$ A, $I_{m2} = 2.00$ A condition has 85% of its magnetic field strength and the $I_{m1} = 1.75$ A, $I_{m2} = 1.75$ A case has 50% of the field strength. Despite the change in field strength, the shape of the radial field profile remains similar. Figure 5 shows the normalized radial field profiles along the acceleration channel centerline calculated using a commercial software simulation package.

In addition to the previously used configurations, an extra condition was tested which attempted to minimize the divergence of the beam. The magnet currents were tuned to maximize the current collected by the Faraday probe at a location of $r = 80$ cm and $\theta = 5^\circ$ for each propellant. The tuned magnet configurations were $I_{m1} = 1.07$ A, $I_{m2} = 2.45$ A for xenon and $I_{m1} = 0.56$ A, $I_{m2} = 2.16$ A for krypton (tuned in flow-matched setting). (These configurations are referred to as ϕ_{DIV} *optimized* in the text and figures.)

For each xenon propellant operating condition, two corresponding krypton propellant operating conditions were tested as in Ref. 9. One condition matched anode volumetric flow rate and therefore particle flux through the anode. The other condition matched anode power. Here the anode flow rate was increased to compensate for the smaller anode current per volumetric flow rate observed when operating with krypton propellant.

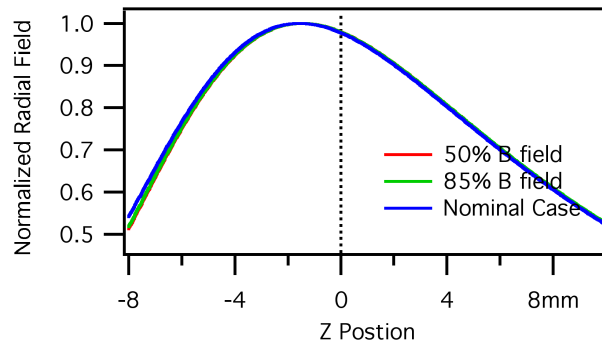


Figure 5. Normalized radial magnetic field strength along the acceleration channel centerline. The radial field strength is a factor of two greater in the high strength case than in the low case. However, the profile of the radial field strength is nearly identical between both cases.

Guarded Faraday Probe

For most operating conditions, guarded Faraday probe sweeps were taken in radial increments of 10 cm from $r = 20$ cm to $r = 80$ cm. The angular range of the sweeps was from $\theta = -120^\circ$ to $\theta = 120^\circ$. Measurements were taken with a 1° angular resolution.

At each radius a value for beam current and beam divergence efficiency were calculated using equations 3 and 4 integrated from -90° to 90° . These calculated values were observed to have a dependency on radius. This dependency was stronger for beam divergence than total beam current. The calculated beam divergence efficiency value was observed to decrease linearly with increasing radius. This phenomenon was likely due to collisions in the plume which led to defocusing. Integrated beam current slightly increased linearly with increasing radius. The greater population of slowly moving charge-exchange ions at higher radii may have artificially increased current to the negatively biased probe. Several calculated beam current values for xenon significantly deviated from the trend of the other data points. Linear extrapolation of the data to the cathode plane ($r = 2$ cm) was used to arrive at representative values of beam current and beam divergence efficiency for each operating condition. This study differs from most other studies in that Faraday probe data was taken at multiple radii.

Table 2 summarizes test operating conditions and tabulates the calculated values of beam current and divergence efficiency. Figures 6, 7, and 8 show the charge flux data and the calculated values of beam current and divergence efficiency for xenon and krypton power-matched cases. In general, the integrated beam current values were higher than expected. This discrepancy is believed to be related to uncertainty in the effective area of the Faraday probe current collector. This type of systematic error would result in inaccuracy by a consistent factor throughout the data. However, due to the mathematics, it would not affect the calculation of divergence angle nor the relative comparison of beam current and current utilization efficiency between cases.

Figure 6 shows Faraday probe results for xenon. The ϕ_{DIV} optimized magnet current setting and the $I_{m1} = 1.75$ A, $I_{m2} = 1.75$ A case both resulted in the best beam focusing while the $I_{m1} = 4.00$ A, $I_{m2} = 2.00$ A case had the most divergence. However, in beam current, the results show a reversal in ranking among the cases where the ϕ_{DIV} optimized case produced the lowest current. In terms of both current utilization and beam divergence, the $I_{m1} = 4.00$ A, $I_{m2} = 2.00$ A case performs the least efficiently. Factoring both the current utilization and beam divergence efficiencies, the best performing configurations were the $I_{m1} = 1.75$ A, $I_{m2} = 1.75$ A (least divergence) and the $I_{m1} = 4.00$ A, $I_{m2} = 4.00$ A (best current utilization) cases.

The krypton power-matched data is shown in Fig. 7. For krypton, the best beam focusing was produced by the ϕ_{DIV} optimized magnet current setting in both the power-matched and volumetric flow rate cases. The inverse relationship between divergence efficiency and total beam current observed for xenon was also seen in the krypton data. While the $I_{m1} = 4.00$ A, $I_{m2} = 2.00$ A case produced the least current utilization efficiency in xenon, it provided the highest value in the case of krypton. Trends in the data were similar between the flow-matched and power-matched cases. In general, the power-matched cases produced higher efficiencies compared to the flow-matched cases suggesting that further increases in mass flow rate may improve krypton performance.

The xenon and krypton data are compared in Fig. 8. Xenon is observed to have about a 17 % divergence efficiency advantage compared to krypton and also better propellant mass utilization efficiency. The higher beam currents for xenon also suggest that xenon has a better propellant utilization efficiency (which factors into thrust and specific impulse calculations). However, due to a lack of charge species population data, the propellant mass utilization advantage cannot be quantified precisely.

Table 2. Faraday probe derived quantities.

I_m Config.		Prop.	Match	\dot{m}_a (mg/s)	P (W)	I_a (A)	I_b (A)	$\frac{I_b}{I_a}$	$\frac{I_b}{I_a}$ Rel. to Xe	ϕ_{DIV} Rel. to Xe	ϕ_{DIV} Rel. to Xe	$\langle \theta \rangle_j$ deg.
I_{m1} (A)	I_{m2} (A)											
1.07	2.45	Xe		2.50	582	1.94	1.833	0.945		0.795		26.9
0.56	2.16	Kr	\dot{V}_a	1.59	495	1.65	1.419	0.860	-9%	0.653	-18%	36.1
0.56	2.16	Kr	P	1.81	582	1.94	1.706	0.879	-7%	0.671	-16%	35.0
		Xe		2.50	579	1.93	1.844	0.955		0.794		27.0
1.75	1.75	Kr	\dot{V}_a	1.59	504	1.68	1.507	0.897	-6%	0.645	-19%	36.6
		Kr	P	1.77	579	1.93	1.738	0.900	-6%	0.653	-18%	36.1
		Xe		2.50	609	2.03	1.877	0.925		0.765		29.0
4.00	2.00	Kr	\dot{V}_a	1.59	504	1.68	1.573	0.937	+1%	0.634	-17%	37.2
		Kr	P	1.84	609	2.03	1.912	0.942	+2%	0.641	-16%	36.8
		Xe		2.50	579	1.93	1.901	0.985		0.773		28.4
4.00	4.00	Kr	\dot{V}_a	1.59	522	1.74	1.544	0.887	-10%	0.649	-16%	36.3
		Kr	P	1.77	579	1.93	1.794	0.929	-6%	0.658	-15%	35.8

Retarding Potential Analyzer

Ion energy-per-charge (eV/q) distribution functions (EDF's) were measured for each case with a retarding potential analyzer at radii of 40 cm and 80 cm. Data was taken in 5° increments from $\theta = -120^\circ$ to $\theta = 120^\circ$. Voltage on the ion retarding grid was swept between 0 and 500 V in 2 V increments relative to chamber ground. The difference between the local plasma potential of the measurement location and chamber was expected to be less than 1% of the anode voltage. This offset was neglected in energy distribution calculations. Each current-voltage trace was individually fitted with a smoothing spline before being differentiated to calculate the ion energy distribution function. Each EDF was area normalized to unity and a mean energy was calculated. The EDF data at 40 cm matched closely with 80 cm for all operating conditions.

Figure 9(a) shows the EDF's for xenon propellant at a radius of 80 cm for various angular locations. At $\theta = 0^\circ$, a primary beam ion energy peak is observed near the anode potential. The highest energy peak is for the $I_{m1} = 4.00$ A, $I_{m2} = 4.00$ A case at 290 eV and the lowest peak occurs at 268 eV for the ϕ_{DIV} optimized case. As theta increases, low energy features appear in the EDF's. At $\theta = 45^\circ$ a significantly higher fraction of low energy ions exist for the $I_{m1} = 1.75$ A, $I_{m2} = 1.75$ A case and the ϕ_{DIV} optimized case than for the $I_{m1} = 4.00$ A, $I_{m2} = 2.00$ A case. This trend seems to correlate with the divergence efficiency data from the Faraday probe as the more focused configurations produce less high energy ions at high angles. At $\theta = 75^\circ$ and $\theta = 90^\circ$ the EDF's are dominated by low energy peaks. However, a small fraction of primary ions is still observed near anode potential. Figure 9(b) displays the trend of the EDF mean over angular position. At high angles, the relationship between plume divergence and distribution mean is apparent. The more divergent beams exhibit higher mean energy.

Krypton energy distribution functions are shown in Fig. 10(a). For krypton, the spread of energy peaks among the different cases at $\theta = 0^\circ$ was smaller than for xenon. Opposite of xenon, the ϕ_{DIV} optimized case had the highest energy peak at 280 eV. The lowest peak was at 270 eV, occurring for the $I_{m1} = 4.00$ A, $I_{m2} = 4.00$ A case. Mean energy data in Fig. 10(b) shows the same relationship between plume divergence and mean energy distribution observed for xenon also applies to krypton.

Krypton and xenon EDF's are plotted together in Fig. 11. One of the most noticeable differences between xenon and krypton EDF's is that krypton has a narrower primary energy peak indicating a smaller spread in primary ion energy. Also due to the higher divergence of krypton, a larger relative population of high energy ions is found at high angles as seen in the $\theta = 60^\circ$ and $\theta = 75^\circ$ EDF plots.

Voltage utilization efficiency was calculated using Eq. 5, where the EDF distribution mean was ion acceleration voltage. The voltage utilization efficiency was calculated twice for each operating condition

using Faraday probe and RPA data from both 40 cm and 80 cm. These two separately calculated values provide an indication of repeatability of this technique for calculating voltage utilization efficiency from probe data.

The approach taken to evaluate voltage utilization efficiency in this study is different than the more common method of only using the ratio of most probable energy to anode voltage.^{3,9,10} Other researchers use the most probable energy approach because probe noise uncertainty results in inaccurate integration of the energy distribution function.⁹ Therefore, the calculated mean energy is less representative of the voltage utilization than the most probable energy.³ However, RPA measurements in this study were found to be highly repeatable, similar for both 40 cm and 80 cm radius at a constant angular location, and symmetrical about $\theta = 0^\circ$. Although, systematic uncertainty exists in these measurements, uncertainty from random noise appeared to be low. In this study, voltage utilization is intended to be used as a comparison metric among cases rather than a figure used in calculating total anode efficiency.

Table 3 contains the calculated values of voltage utilization efficiency for each case. Calculations for the different radii were highly repeatable with less than 2% deviation. For xenon, the best voltage utilization efficiency was calculated for the $I_{m1} = 4.00$ A, $I_{m2} = 4.00$ A case. In general, power-matched krypton cases produced higher voltage utilization efficiency compared to the flow-matched cases. The $I_{m1} = 4.00$ A, $I_{m2} = 2.00$ A case produced the best voltage utilization efficiency for krypton. Voltage utilization efficiency appeared to be higher for cases with higher beam current.

Table 3. RPA Derived Quantities

I_m Config.		Prop.	Match	\dot{m}_a (mg/s)	P (W)	I_a (A)	$\frac{\Delta V}{V_a}$ (40 cm)	rel. to Xe	$\frac{\Delta V}{V_a}$ (80 cm)	rel. to Xe
I_{m1} (A)	I_{m2} (A)									
1.07	2.45	Xe		2.50	582	1.94	0.761		0.775	
0.56	2.16	Kr	\dot{V}_a	1.59	495	1.65	0.785	3%	0.782	1%
0.56	2.16	Kr	P	1.81	582	1.94	0.799	5%	0.779	1%
1.75	1.75	Xe		2.50	579	1.93	0.814		0.819	
		Kr	\dot{V}_a	1.59	504	1.68	0.743	-9%	0.749	-8%
		Kr	P	1.77	579	1.93	0.806	-1%	0.806	-2%
4.00	2.00	Xe		2.50	609	2.03	0.784		0.793	
		Kr	\dot{V}_a	1.59	504	1.68	0.741	-5%	0.744	-6%
		Kr	P	1.84	609	2.03	0.814	4%	0.806	2%
4.00	4.00	Xe		2.50	579	1.93	0.836		0.823	
		Kr	\dot{V}_a	1.59	522	1.74	0.737	-12%	0.737	-10%
		Kr	P	1.77	579	1.93	0.799	-4%	0.783	-5%

Discharge Current Oscillation Effects

Anode current data was measured in the time domain using an oscilloscope and in the frequency domain using a signal analyzer for all tested operating conditions. Magnet current settings were observed to strongly influence oscillatory behavior of anode current. Figure 12 shows the anode current behavior for xenon. Both the $I_{m1} = 1.75$ A, $I_{m2} = 1.75$ A and the ϕ_{DIV} optimized case were observed to have a highly oscillatory nature and harmonic frequencies. The most quiescent case was the $I_{m1} = 4.00$ A, $I_{m2} = 4.00$ A. The peak frequency was highest for the quiescent case (41.1 kHz) and decreased as the oscillation magnitude increased (37.2 kHz for the ϕ_{DIV} optimized case).

Figure 13 shows the anode current oscillations for the krypton power-matched cases and Fig. 14 displays this same data along with the xenon data for comparison. Overall, the krypton oscillation magnitudes were much smaller than for xenon. Similar to xenon, the krypton ϕ_{DIV} optimized case produced the largest magnitude oscillations. The $I_{m1} = 4.00$ A, $I_{m2} = 2.00$ A case was most quiescent. However, in contrast to xenon the most quiescent krypton cases had the lowest peak frequency (20.5 kHz) and peak frequency increased with increasing oscillation magnitude (41.6 kHz for the divergence optimized case).

Table 4 summarizes the anode current data for all the operating conditions. The beam current appears to be strongly related to the anode current oscillations. For xenon, high beam current cases tend to have low oscillation magnitudes and high peak frequency. Whereas for krypton, high beam current cases tend to have both low oscillation magnitude and low peak frequency. Consequently, low divergence cases (having low beam current) produce large anode oscillations.

Table 4. Anode Current Data

I_m Config.		Prop.	Match	\dot{m}_a (mg/s)	P (W)	I_a (A)	I_b (A)	$\frac{I_b}{I_a}$	ϕ_{DIV}	$\frac{\Delta V}{V_a}$ (80 cm)	σ_{I_a} (A)	f_{peak} (kHz)	P_{I_d} (dB-A)
I_{m1} (A)	I_{m2} (A)												
1.07	2.45	Xe		2.50	582	1.94	1.833	0.945	0.795	0.775	0.78	37.2	-18.9
0.56	2.16	Kr	\dot{V}_a	1.59	495	1.65	1.419	0.860	0.653	0.782	0.23	37.5	-34.6
0.56	2.16	Kr	P	1.81	582	1.94	1.706	0.879	0.671	0.779	0.18	41.6	-43.4
1.75	1.75	Xe		2.50	579	1.93	1.844	0.955	0.794	0.819	0.80	36.4	-18.1
		Kr	\dot{V}_a	1.59	504	1.68	1.507	0.897	0.645	0.749	0.12	24.5	-45.3
		Kr	P	1.77	579	1.93	1.738	0.900	0.653	0.806	0.12	27.2	-47.2
4.00	2.00	Xe		2.50	609	2.03	1.877	0.925	0.765	0.793	0.45	40.3	-32.9
		Kr	\dot{V}_a	1.59	504	1.68	1.573	0.937	0.634	0.744	0.05	19.7	-43.9
		Kr	P	1.84	609	2.03	1.912	0.942	0.641	0.806	0.05	20.5	-53.7
4.00	4.00	Xe		2.50	579	1.93	1.901	0.985	0.773	0.823	0.24	41.1	-43.7
		Kr	\dot{V}_a	1.59	522	1.74	1.544	0.887	0.649	0.737	0.09	22.0	-43.9
		Kr	P	1.77	579	1.93	1.794	0.929	0.658	0.783	0.07	23.3	-48.3

Conclusion

This investigation compared plume data from a medium power Hall effect thruster operating with xenon and krypton propellant. Faraday probe data was used to calculate divergence efficiency, beam current, and beam current utilization efficiency. Energy-per-charge distribution functions, measured with an RPA, were used to calculate voltage utilization efficiency. Anode current data were analyzed in the frequency domain to correlate oscillatory behavior with beam properties.

The methodology of this plume study was different than typical performance analysis studies in two ways. First, probe data was taken at multiple radii. Faraday probe data were typically taken between 7 (for Kr testing) and 13 (for Xe testing) different radii. Divergence efficiency was observed to exhibit a strong linear relationship with probe sweep radius. Retarding potential analyzer data was taken at two radii for each operating condition. Energy-per-charge distribution functions remained similar at both radii.

The second difference was that charge-weighted integration of mean energy was used to calculate voltage utilization efficiency instead of using only the most probable energy from EDF's measured near $\theta = 0^\circ$. This method of calculation is more analytically rigorous, but is possibly subject to greater uncertainty from integrating EDF's that have higher uncertainties at low energy. A more detailed study on the accuracy of RPA derived EDF's for a medium power Hall thruster will have to be conducted to determine which voltage utilization efficiency calculation technique is most appropriate.

Faraday probe data revealed that krypton has a divergence efficiency value approximately 15-20% less than xenon. It also showed that krypton current utilization efficiency is 5-10% less than that of xenon. Different radial magnetic field strength configurations had a significant effect on divergence and current efficiency values.

Differences between voltage utilization efficiency for xenon and krypton were small (approximately 2% less for krypton). Voltage utilization efficiency was observed to be linked to beam current, where cases with higher beam current had higher voltage utilization efficiency. Retarding potential analyzer data showed that significant populations of high energy ions existed at high angles for operating conditions with high divergence.

Different magnetic fields produced variations in anode current oscillatory behavior. Anode current oscillation magnitude was observed to be significantly smaller for krypton than xenon. Operating conditions with high beam current tended to produce larger magnitude oscillations. For xenon, peak frequency decreased with oscillation magnitude, but for krypton the opposite effect was observed.

Besides the efficiency losses studied here (relating to anode efficiency), the propellant mass utilization efficiency (\dot{m}_i/\dot{m}_a) appeared to be significantly less for krypton. The propellant mass utilization efficiency cannot be calculated accurately without charge species fractions and was not quantified due to the lack of $E \times B$ data in this study. Specific impulse is directly proportional to mass utilization efficiency. Losses in mass utilization efficiency would directly counteract the prized high ion velocity of krypton in the calculation of specific impulse. Considering this loss combined with the higher beam divergence loss, the specific impulse for krypton may not be better for krypton than xenon for this medium power Hall thruster.

Ultimately, a more thorough experimental study that includes charge species measurements from an $E \times B$ probe and thrust data from a thrust stand is needed to make more complete and accurate evaluations of the anode efficiency and thruster performance. Also, a more rigorous survey of operating conditions that includes increasing anode flow rate and discharge potential should be performed to find operating conditions that maximize the efficiency and performance of krypton. These conditions would provide more relevant comparisons to the established xenon operating conditions. Initial observations for a limited number of operating cases indicate that krypton is significantly less efficient than xenon and likely does not offer a significant increase in specific impulse for the BHT-HD-600 Hall thruster.

Appendix: Experimental Data Figures

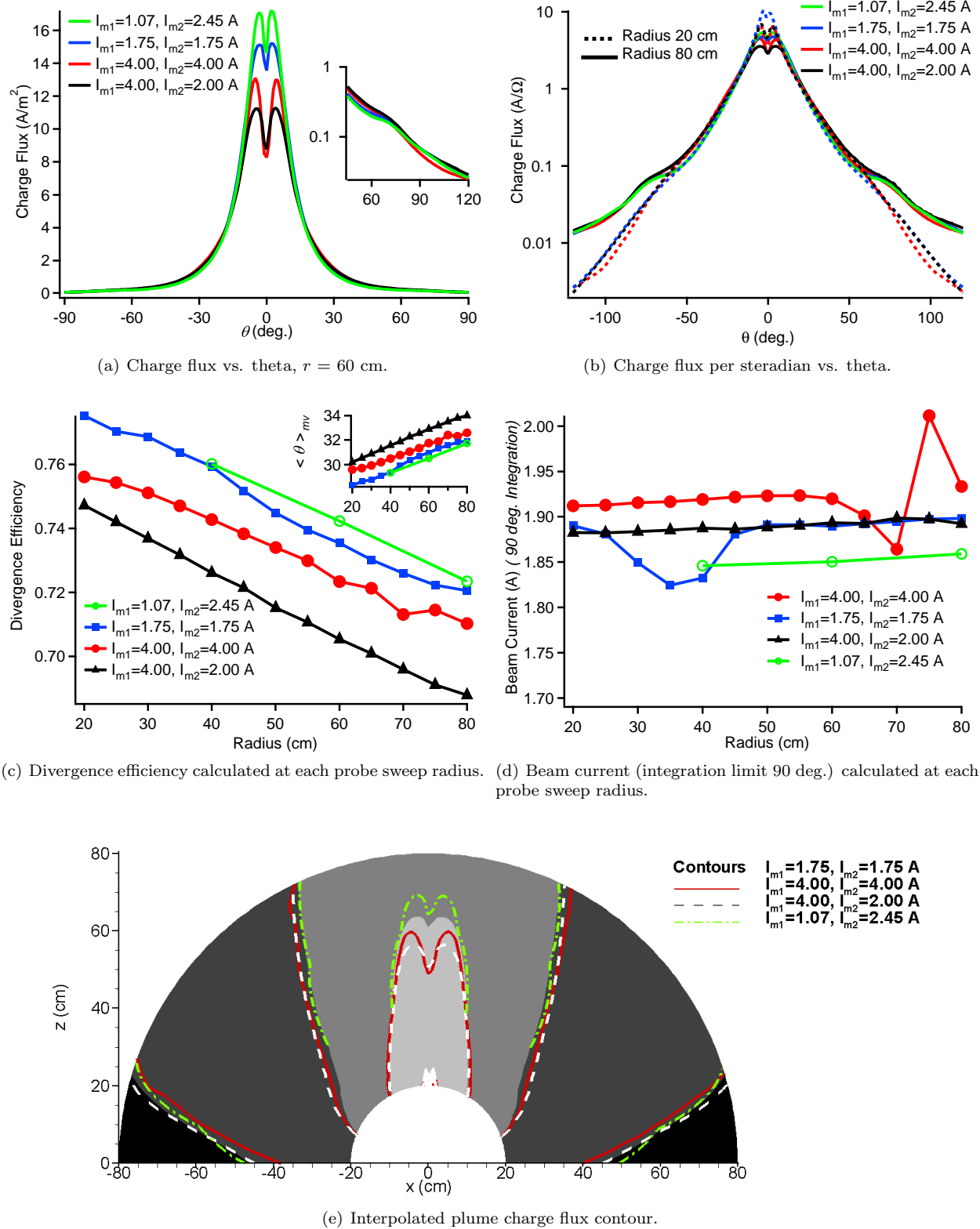
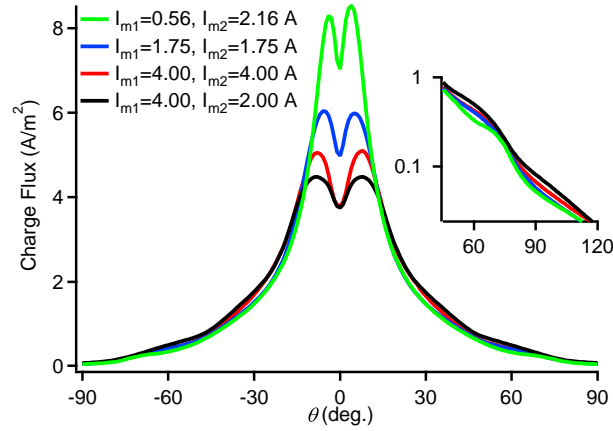
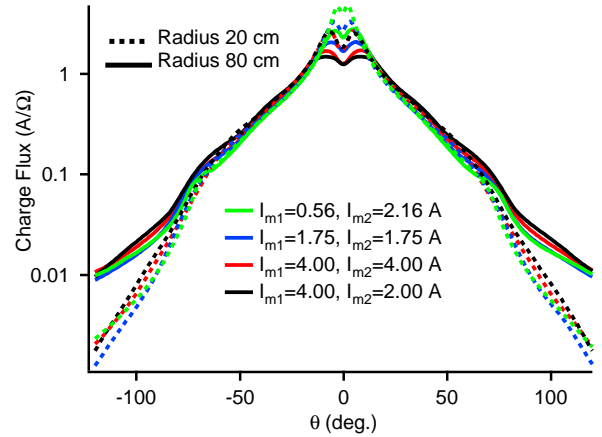
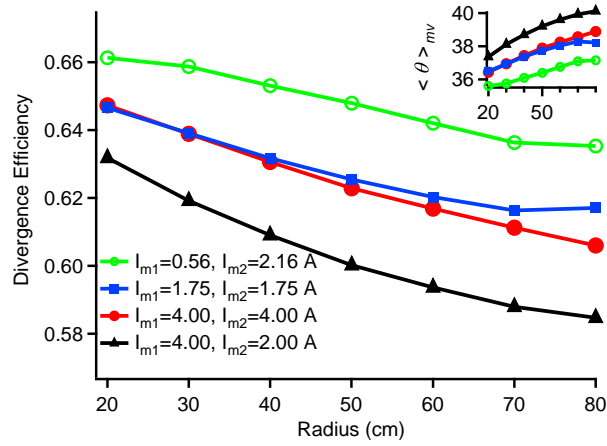


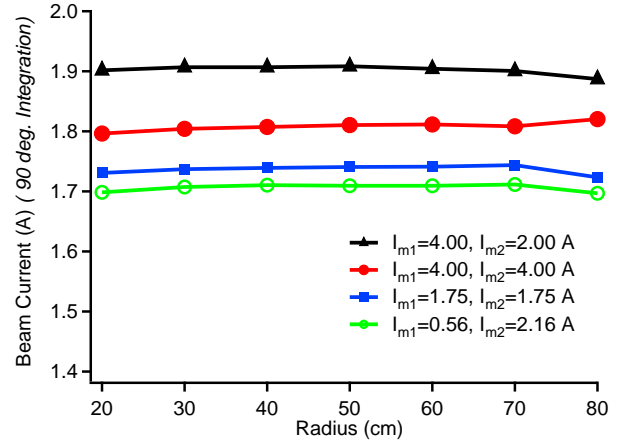
Figure 6. *Xenon Magnet Current Comparison: Faraday probe data for thruster operating at $V_d=300$ V, and $\dot{m}_a=25.5$ sccm.*

(a) Charge flux vs. theta, $r = 60$ cm.

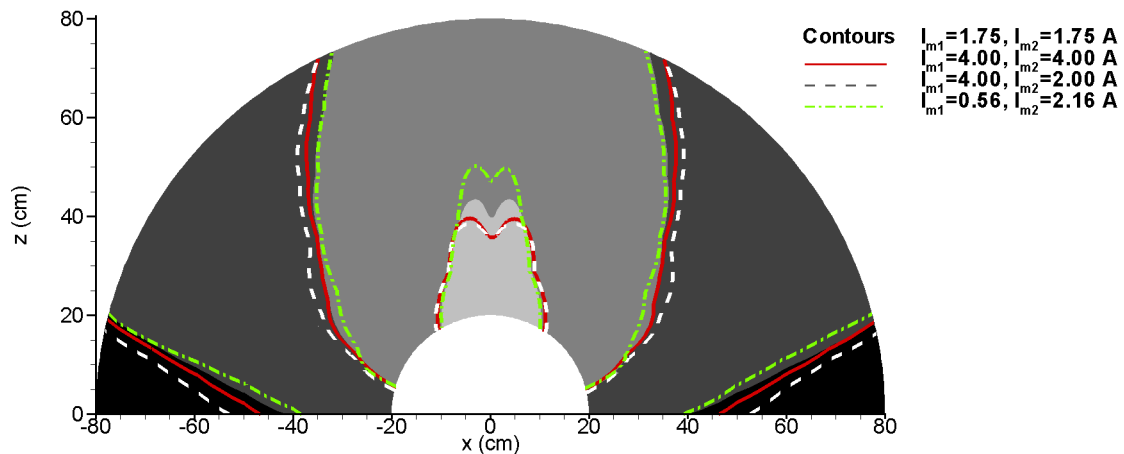
(b) Charge flux per steradian vs. theta.



(c) Divergence efficiency calculated at each probe sweep radius.



(d) Beam current (integration limit 90 deg.) calculated at each probe sweep radius.



(e) Interpolated plume charge flux contour.

Figure 7. *Krypton(power matched) Magnet Current Comparison: Faraday probe data for thruster operating at $V_d=300$ V.*

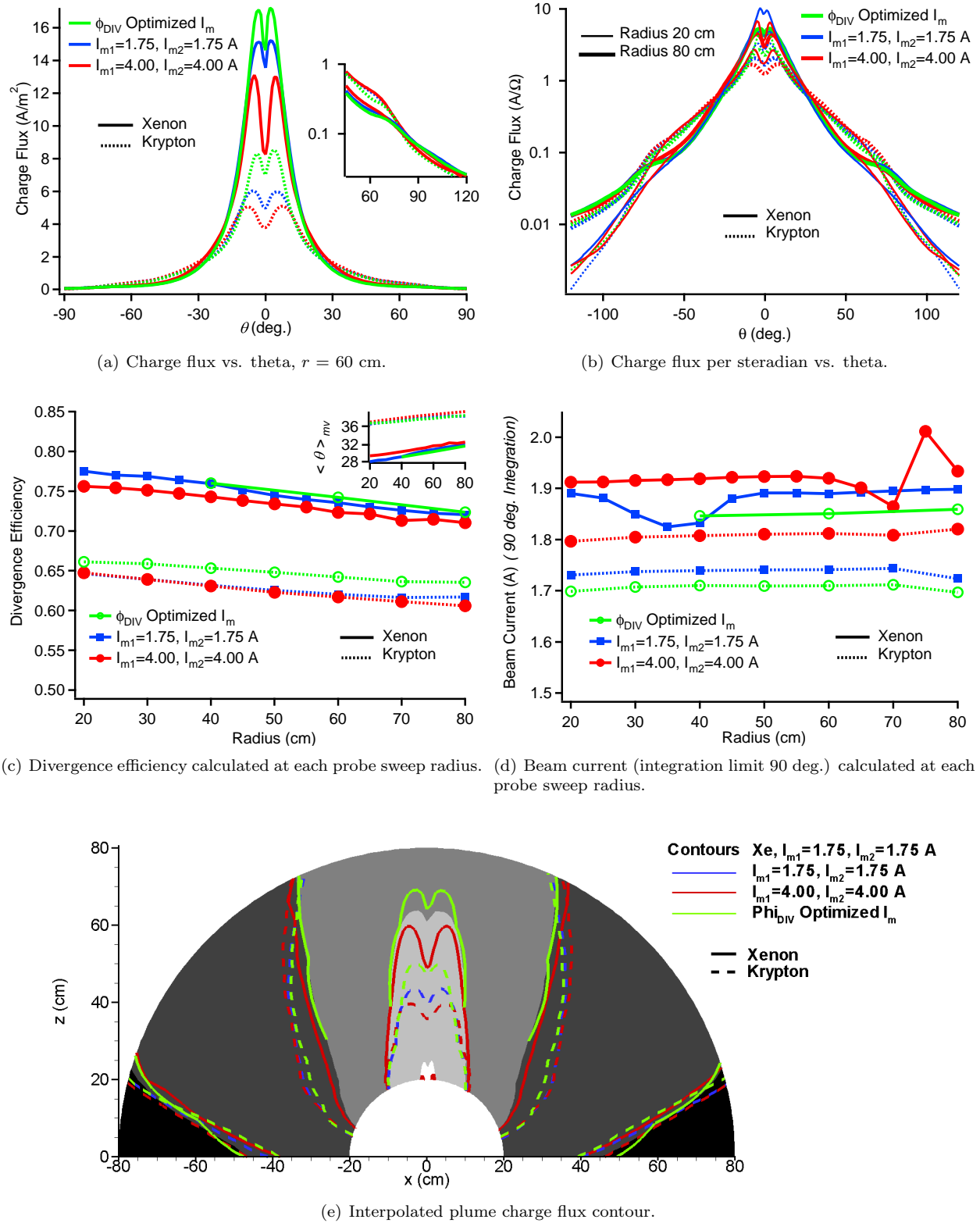
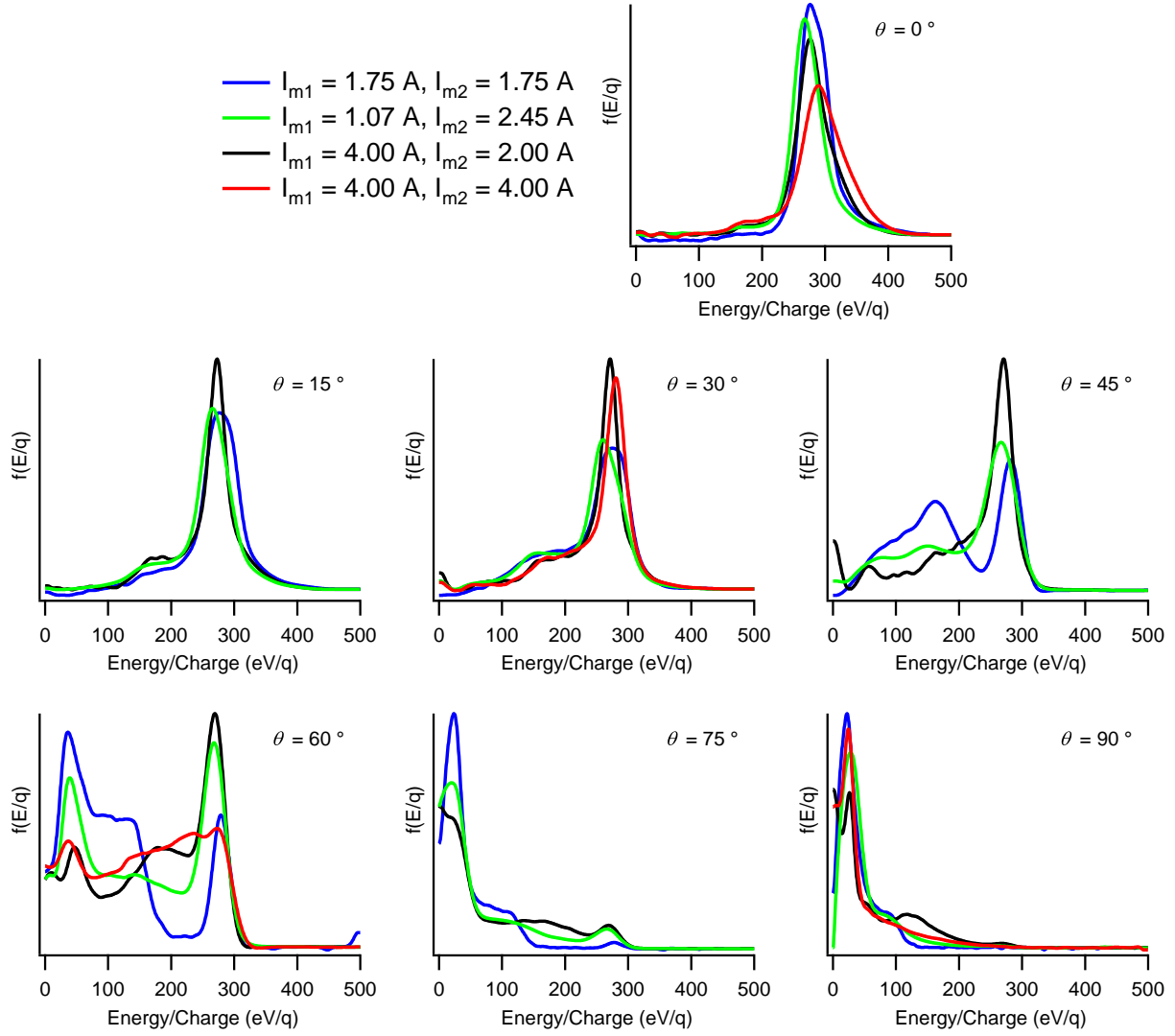
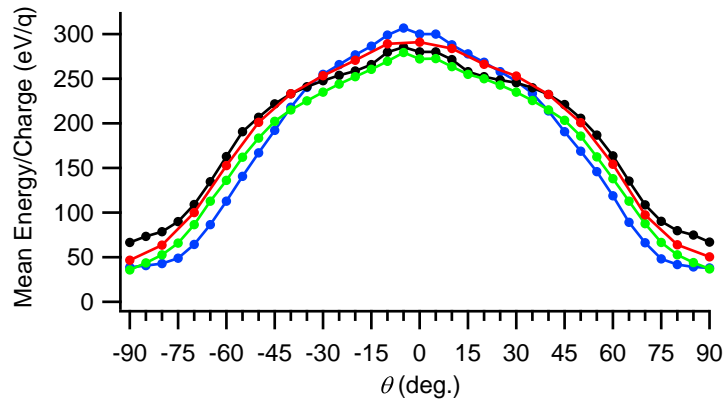
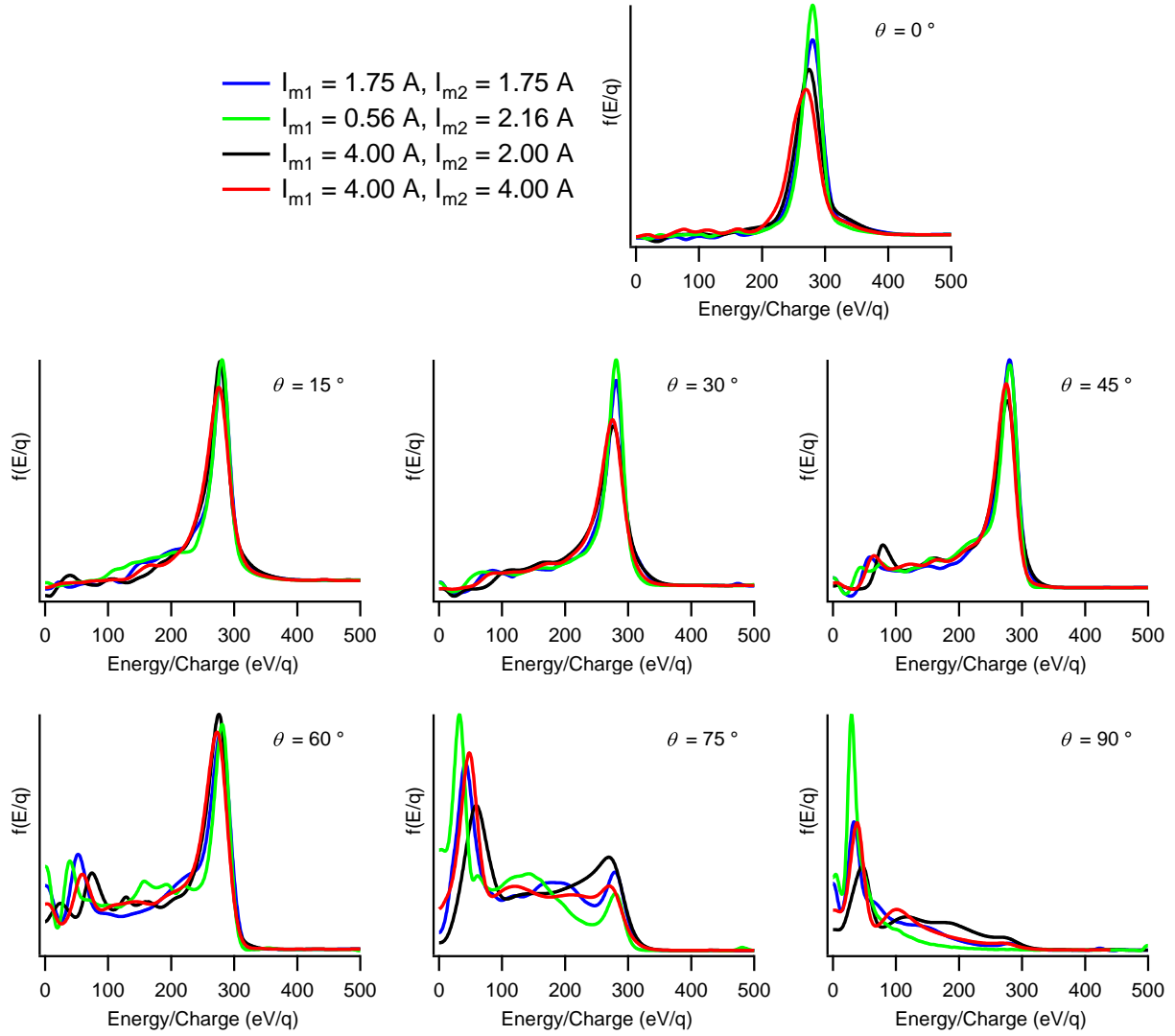
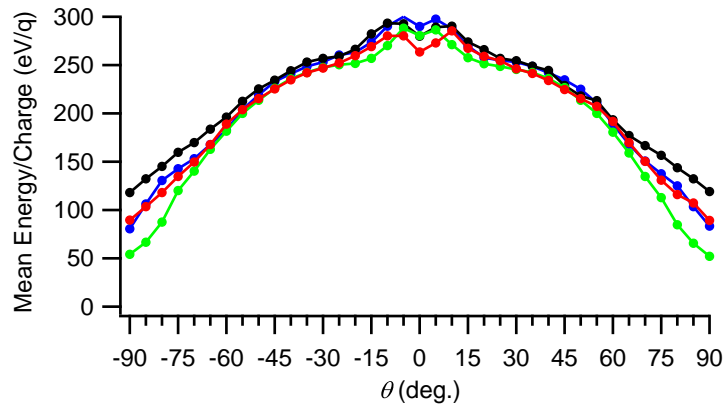


Figure 8. *Xenon vs. Krypton (power matched) Magnet Current Comparison: Faraday probe data for thruster operating at $V_d=300$ V.*

(a) Energy Distribution Function, $r = 80 \text{ cm}$ (b) Energy Distribution Function Mean Values, $r = 80 \text{ cm}$ **Figure 9. Xenon Magnet Current Comparison: RPA data for thruster operating at $V_d=300 \text{ V}$, and $\dot{m}_a=25.5 \text{ sccm}$.**

(a) Energy Distribution Function, $r = 80 \text{ cm}$ (b) Energy Distribution Function Mean Values, $r = 80 \text{ cm}$ Figure 10. *Krypton(power matched) Magnet Current Comparison: RPA data for thruster operating at $V_d=300 \text{ V}$.*

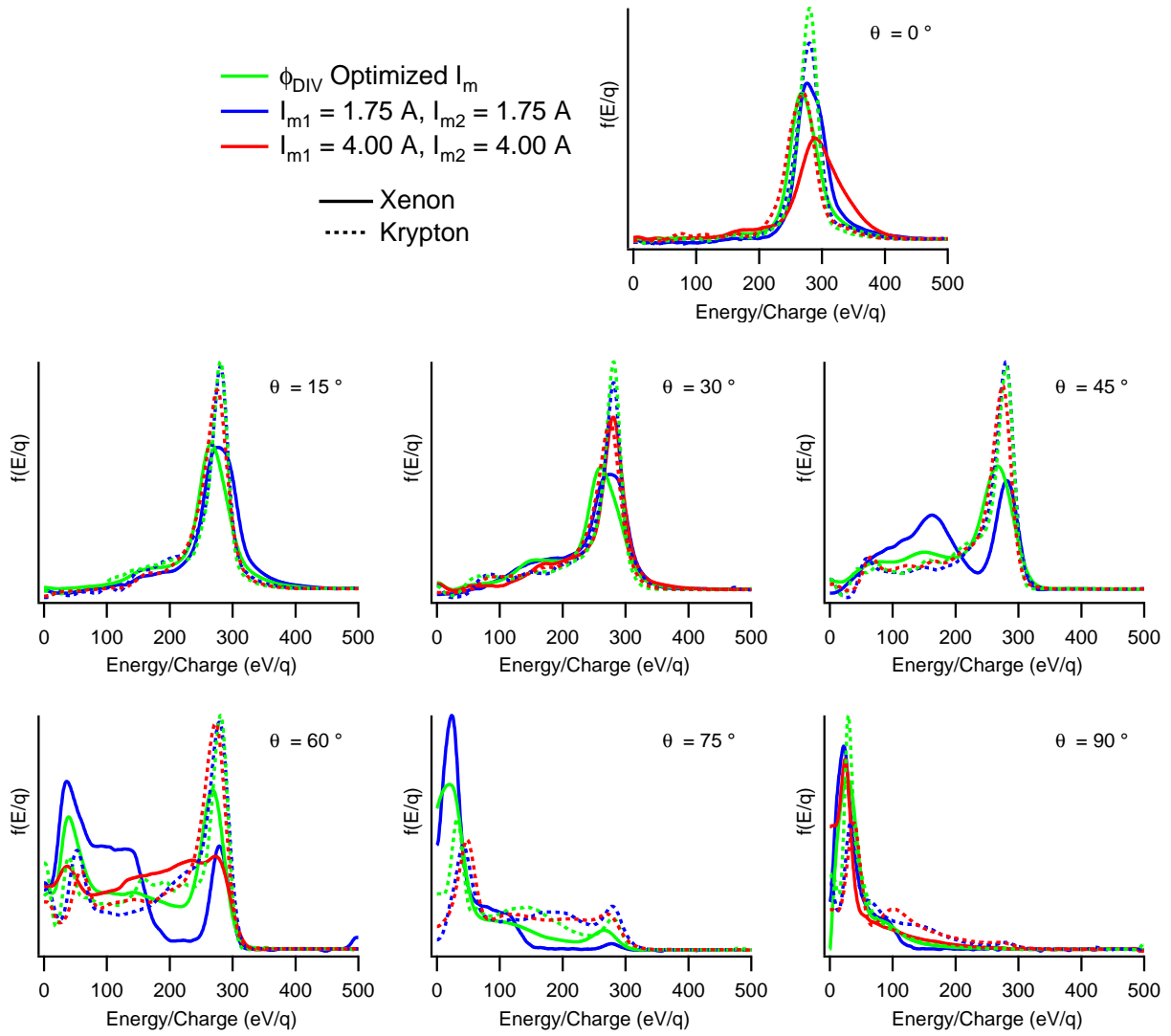
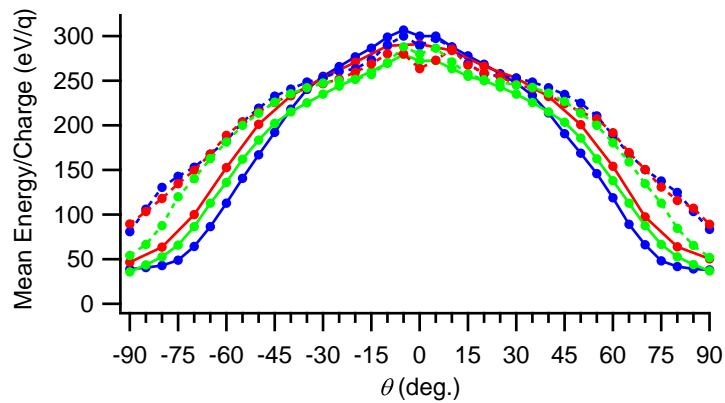
(a) Energy Distribution Function, $r = 80$ cm(b) Energy Distribution Function Mean Values, $r = 80$ cm

Figure 11. *Xenon vs. Krypton (power matched) Magnet Current Comparison: RPA data for thruster operating at $V_d=300$ V.*

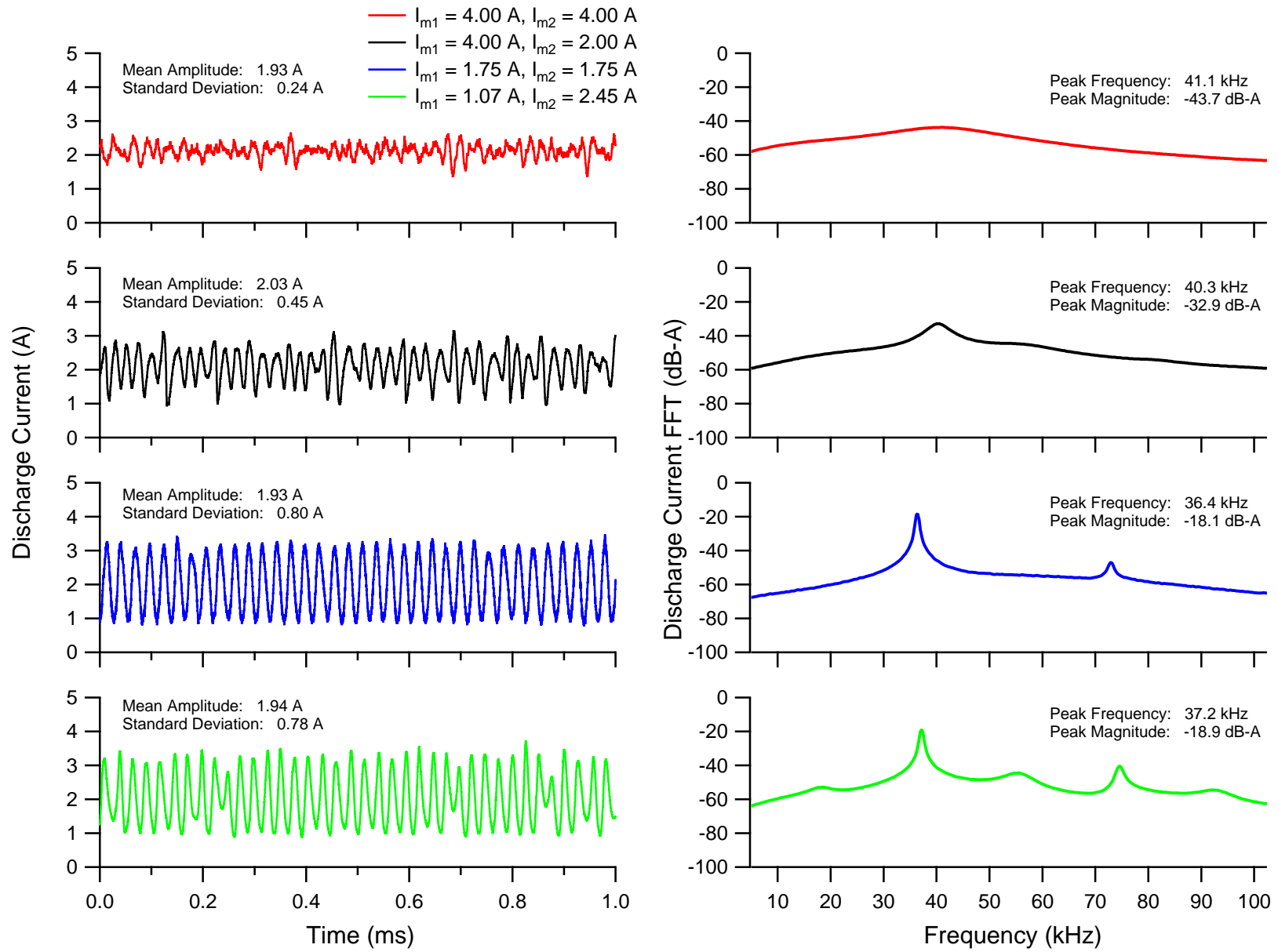


Figure 12. *Xenon Magnet Current Comparison*: Anode current data for thruster operating at $V_d=300$ V, and $\dot{m}_a=25.5$ sccm.

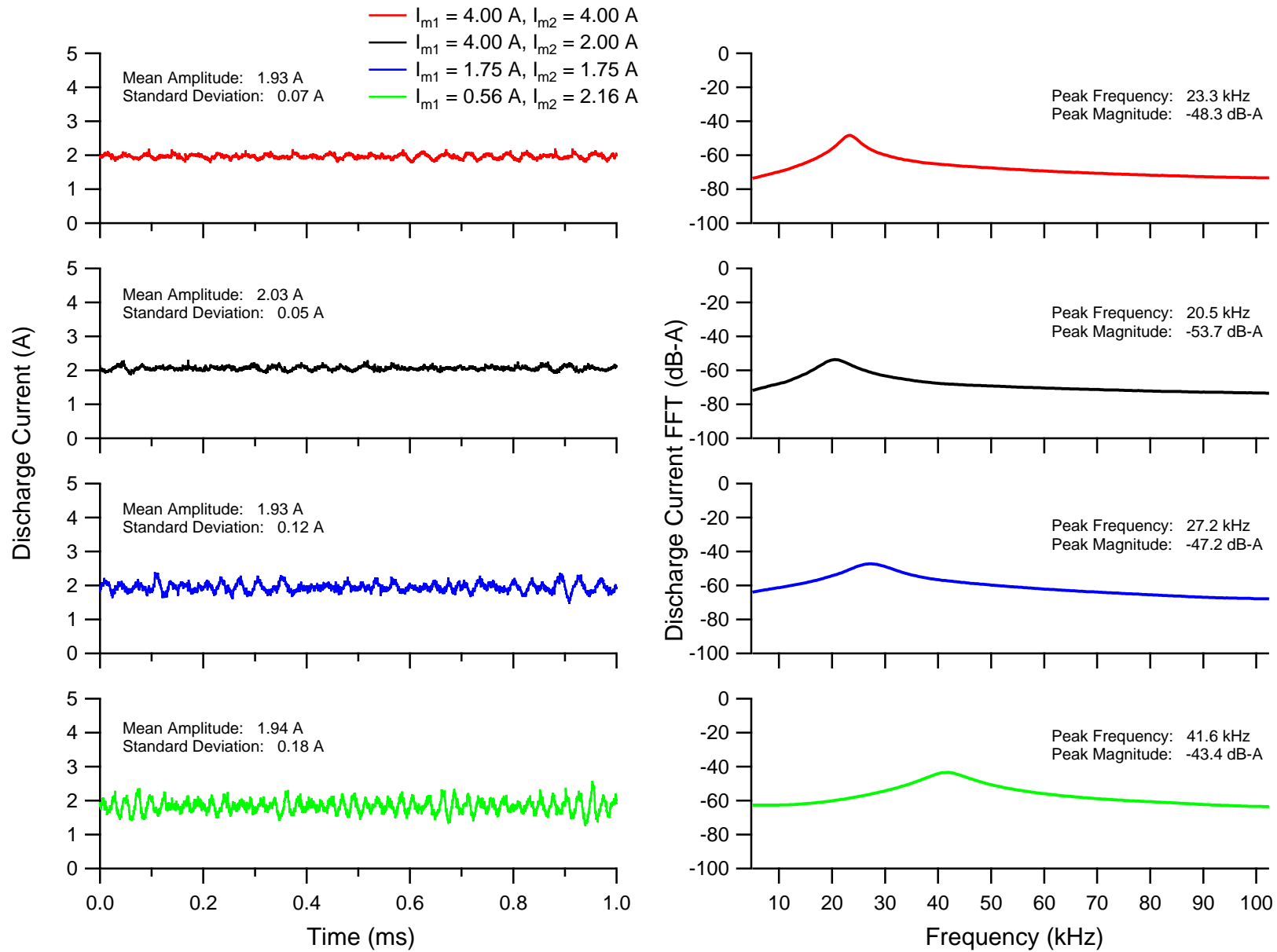


Figure 13. *Krypton (power matched) Magnet Current Comparison: Anode current data for thruster operating at $V_d=300$ V.*

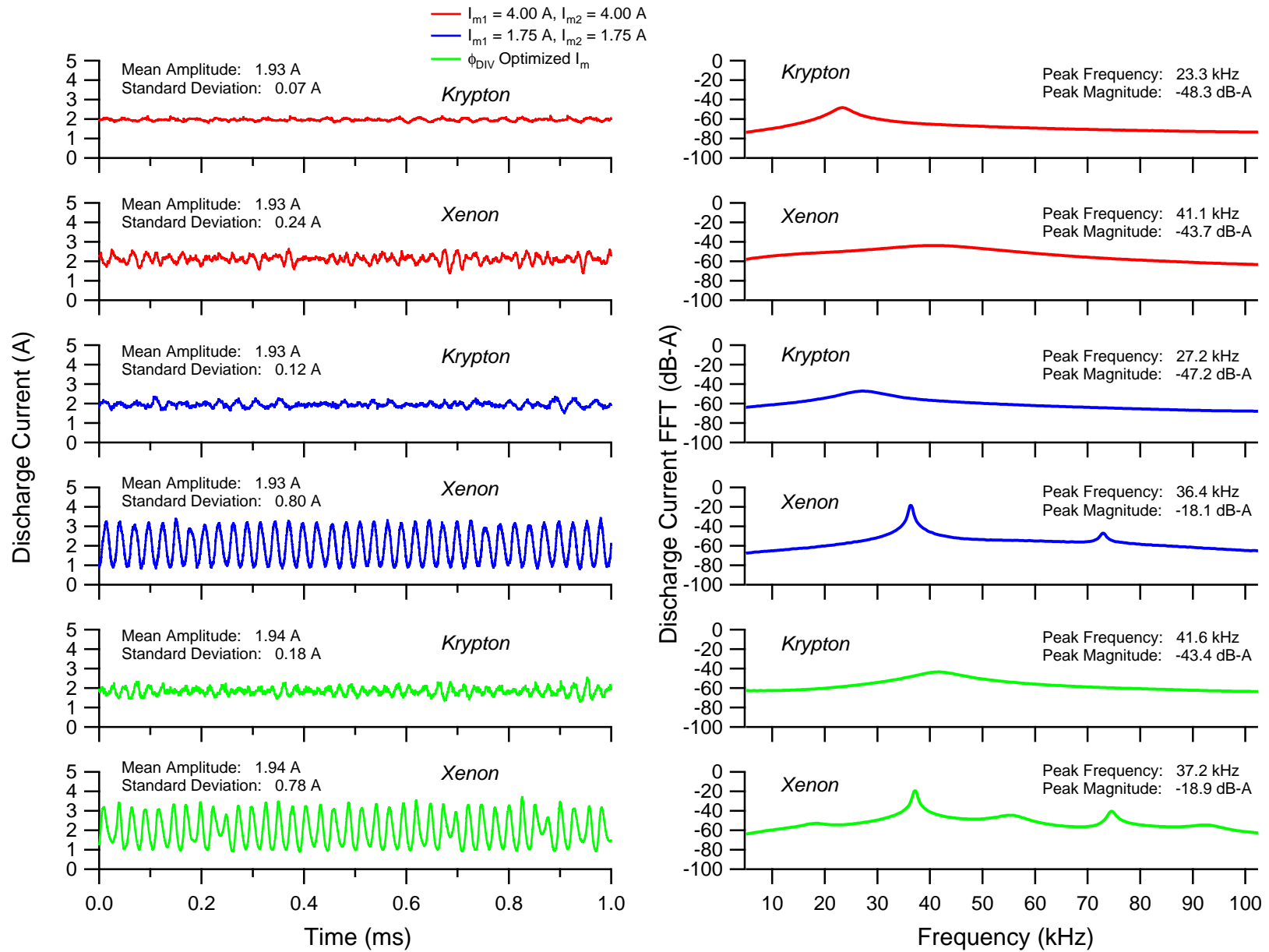


Figure 14. *Xenon vs. Krypton (power matched) Magnet Current Comparison: Anode current data for thruster operating at $V_d=300$ V.*

Acknowledgments

The authors would like to thank Paul Adkinson from AFRL and D. Luke O'Malley from Malibu High School for their help with the mechanical design improvements and assembly of the retarding potential analyzer. Helpful discussions with AFRL engineers Dan Brown, Justin Koo, and Michelle Scharfe contributed to the success of this research. Thanks also go to Stephen Gildea from MIT for assisting with the RPA measurements, Bruce Pote and Rachel Tedrake from Busek for providing thruster magnetic field data, Robert Lobbia from University of Michigan for sharing some of his experimental data, and Sasha MacDonald from Stanford for text editing assistance.

References

- ¹Larson, C. W., Brown, D. L., and Hargus Jr., W. A., "Thrust Efficiency, Energy Efficiency and the Role of VDF in Hall Thruster Performance Analysis," *Proceedings of the 43rd AIAA/ASME/SAE/ASEE Joint Propulsion Conference & Exhibit*, Cincinnati, OH, July 2007, AIAA-2007-5270.
- ²Duchemin, O., Valentian, D., and Cornu, N., "Cryostorage of Propellants for Electric Propulsion," *45th AIAA/ASME/SAE/ASEE Joint Propulsion Conference*, No. AIAA-2009-4912, Denver, CO, 2009.
- ³Brown, D. L., *Investigation of Low Discharge Voltage Hall Thruster Characteristics and Evaluation of Loss Mechanisms*, Ph.D. thesis, University of Michigan, 2009.
- ⁴Brown, S. C., *Basic Data of Plasma Physics*, American Institute of Physics Press, New York, 1994.
- ⁵Hutchinson, I., *Principles of Plasma Diagnostics*, Cambridge University Press, New York, 1994.
- ⁶Hargus Jr., W. A., Nakles, M. R., Pote, B., and Tedrake, R., "Effect of Anode Current Fluctuations on Ion Energy Distributions within a 600 W Hall Effect Thruster," *Proceedings of the 44th Joint Propulsion Conference and Exhibit*, No. AIAA-2008-4724, American Institute of Aeronautics and Astronautics, Hartford, CT, July 2008.
- ⁷Nakles, M. R. and Hargus Jr., W. A., "Background Pressure Effects on Internal and Near-Field Ion Velocity Distribution of the BHT-600 Hall Thruster," *Proceedings of the 44th Joint Propulsion Conference and Exhibit*, No. AIAA-2008-5101, American Institute of Aeronautics and Astronautics, Hartford, CT, July 2008.
- ⁸Ekholm, J. M., Hargus, Jr., W. A., Larson, C. W., Nakles, M. R., Reed, G., and Niemela, C. S., "Plume Characteristics of the Busek 600 W Hall Thruster," *Proceedings of the 42th AIAA/ASME/SAE/ASEE Joint Propulsion Conference*, No. AIAA-2006-4659, Sacramento, CA, 2006.
- ⁹Linnell, J. A. and Gallimore, A. D., "Efficiency Analysis of a Hall Thruster Operating with Krypton and Xenon," *Journal of Propulsion and Power*, Vol. 22, No. 6, November-December 2006, pp. 1402–1412.
- ¹⁰Hofer, R. R. and Gallimore, A. D., "High-Specific Impulse Hall Thrusters, Part 2: Efficiency Analysis," *Journal of Propulsion and Power*, Vol. 22, No. 4, July-August 2006, pp. 732–740.